High-melting metallic lattice structures fabricated by additive manufacturing assisted investment casting

Yan-peng Wei[1,2], Huai-qian Li[1], Ying-chun Ma[1], Hao-ran Zhou[1], Zhi-quan Miao[1], *Bo Yu[1], and *Feng Lin[2]

1. National Key Laboratory of Advanced Casting Technologies, Shenyang Research Institute of Foundry, Shenyang 110022, PR China.

2. Department of Mechanical Engineering, Tsinghua University, Beijing 100084, PR China.

*Corresponding address: e-mail: linfeng@tsinghua.edu.cn

Abstract: Metallic lattice structures exhibit exceptional multifunctional attributes, including lightweight design, vibration damping, and energy absorption, with transformative potential in aerospace and marine engineering. While additive manufacturing combined with investment casting provides a cost-efficient fabrication route, current implementations predominantly utilize low-melting-point metals, severely restricting their application ranges. High-melting-point metallic lattice structures (e.g., superalloys, steels) surpass conventional counterparts in strength, stiffness, and thermal resistance; however, the lack of compatible preform materials poses a huge challenge to the fabrication of high-melting metallic lattice structures. This study pioneers the first integrated fabrication of high-melting-point metallic lattice structures via additive manufacturing assisted investment casting. A novel quartz glass-based ceramic preform system was engineered, featuring a tailored compositional formulation and sintering protocol to meet high-temperature processing demands. Orthogonal experimentation coupled with finite element simulations optimized casting parameters (1550°C pouring temperature, 900°C mold preheating), while multiscale characterization (ProCAST, micro-CT, metallography) reveals localized shrinkage porosity at nodal junctions-an inherent solidification challenge. Validated cellular automaton finite element (CAFE) modeling further enables grain structure prediction, providing mechanistic insights for solidification control. This methodology establishes a scalable platform for high-performance metallic lattice structures production, overcoming traditional temperature limitations while maintaining geometric fidelity and economic viability for wider applications.

Keywords: High-melting metallic lattice structures; Indirect additive manufacture; Ceramic preform; Investment casting; Finite element simulation.

1 Introduction

Lattice structures are defined as three-dimensionally ordered porous architectures featuring non-stochastic, tailorable geometries[1,2]. Precise control of structural topology and porosity enables systematic tuning of mechanical and functional properties [3]. Metallic lattice structures exhibit superior attributes such as lightweight, high specific strength-to-weight ratios, and vibroacoustic damping capabilities, coupled with energy-absorbing functionalities[4,5]. These unique characteristics have garnered significant recognition within the materials science community, positioning them as leading candidates for advanced lightweight materials [6].

Metallic lattice structures are predominantly fabricated via additive manufacturing, which can be categorized into two principal approaches: direct and indirect additive manufacturing[7,8]. While direct additive manufacturing demonstrates limitations in lattice structures fabrication, three key challenges emerge: (1) compositional adjustments necessitate costly customized powders [9]; (2) surface step artifacts impair dimensional accuracy and mechanical performance in fine-featured

structures[10]; (3) inherent process-induced anisotropy compromises structural uniformity[11,12]. In contrast to direct additive manufacturing, the indirect additive manufacturing approach employs a multi-stage fabrication process: additive manufacturing is first utilized to create polymer-based sacrificial templates patterns, followed by preform formation and investment casting techniques, ultimately yielding high-fidelity metallic lattice architectures. Indirect additive manufacturing can effectively overcome the shortcomings of direct metal additive manufacturing[13,14] and offers significant advantages in material composition selection and surface roughness[15,16]. At the same time, the preparation cost of indirect additive manufacturing is substantially lower[17]. Therefore, indirect additive manufacturing technology exhibits strong competitiveness in the preparation of metallic lattice structures.

It is widely recognized that high-melting-point metallic lattice structures exhibit enhanced strength, stiffness, and thermal stability, thereby substantially expanding their application potential. However, current indirect additive manufacturing methods for fabricating metallic lattice structures[18,19] primarily concentrate on low-melting-point alloys (predominantly aluminum alloy). Fabricating high-melting-point metallic lattice structures (high-temperature superalloys or ferrous materials) via indirect additive manufacturing remains particularly challenging. The preform materials currently employed for low-melting-point systems—including NaCl[11], silica sand[12], and gypsum [19]—suffer from inadequate thermal stability, rendering them unsuitable for high-temperature casting processes. While conventional refractory materials (e.g., α-alumina and yttria-stabilized zirconia) demonstrate sufficient temperature resistance, their persistent structural interlocking with metallic frameworks[20] severely complicates post-casting removal. Consequently, the critical challenge lies in developing thermally stable materials that simultaneously ensure high-temperature integrity and facile removability.

The strategic selection of ceramic preforms constitutes a pivotal challenge in fabricating high-melting-point metallic lattice structures. Three critical criteria govern this selection: (1) minimal coefficient of thermal expansion (CTE), (2) crystalline phase stability during sintering, and (3) post-casting removability[21,22]. An ultra-low CTE ($<1\times10^{-6}$ K^{-1}) ensures dimensional stability during metal infiltration while minimizing residual stress in the final structure [23]. Phase-stable ceramics must resist polymorphic transitions to avoid sintering-induced cracking from volumetric variations[21]. Chemical solubility is essential for complete preform dissolution without damaging the metallic architecture[22]. Drawing from investment casting methodologies, candidate materials were narrowed to α-Al_2O_3, quartz glass (amorphous SiO_2), and β-SiC[24]. Comparative evaluation identified quartz glass as optimal, exhibiting CTE values of $0.51\text{-}0.63\times10^{-6}$ K^{-1}[25,26] combined with superior chemical etchability. Despite these merits, quartz glass's low devitrification threshold (~1,200°C) predisposes it to cristobalite crystallization, mandating precise optimization of binder composition and sintering parameters to maintain structural integrity for successful metal casting operations.

This study pioneers a novel fabrication methodology employing selective laser sintering (SLS) technology to manufacture polystyrene-based sacrificial templates, enabling the development of a high-temperature-resistant ceramic preform derived from amorphous quartz glass. Systematic optimization established the compositional formulation and sintering protocol, ultimately yielding high-fidelity metallic lattice structures via investment casting. Computational modeling using ProCAST software analyzed mold-filling and solidification behavior, with orthogonal experimental design identifying optimal process parameters. Cellular automaton finite element (CAFE) simulations predicted grain evolution and defect distribution, providing microstructure-level insights. The metallic lattice structure with a Kelvin cell was fabricated using IN718 alloy as the matrix material, providing further validation of the simulation results.

2 Experimental section

2.1 Materials

In this work, sacrificial templates for metallic lattice architectures were fabricated via selective laser sintering (SLS). Spherical polystyrene powders (average particle diameter: 100 μm) served as the feedstock material, with the basic physical properties of polystyrene are shown in Table 1.

The ceramic preform matrix in this study comprises quartz glass, formulated into a ceramic slurry via silica sol binder and additives. The slurry composition and mass ratios are detailed in Table 2.

Inconel 713 superalloy—widely adopted in aerospace applications due to its superior creep resistance,

thermal fatigue durability, and oxidation stability below 900°C [27]—was selected as the representative matrix material to evaluate the preform's thermal tolerance and removability. Table 3 lists the alloy's chemical composition.

Table 1 Physical parameters of Polystyrene.

Material	Heat distortion temperature/℃	Softening point/℃	Density /(g/cm³)
Polystyrene	88	94	1.05

Table 2 The components of the ceramic slurry.

Ceramic slurry	Materials	Particle size/Concentration	Content (wt.%)
Matrix material	Quartz glass	320 mesh	53.70
Sintering aids	Kaolin	100 mesh	1.00
	Corundum sand	100 mesh	14.00
Ultrafine powder	micro silicon powder	3000 mesh	1.00
Agglomerant	silica sol	30%	30.00
Defoaming agent	organosilicon	——	0.15
Surfactant	JFC	——	0.15

Table 3 Chemical composition of Inconel 713 (wt.%).

C	Cr	Co	Al	Nb	Fe	Mo	Ti	Ni
0.13	13.90	0.15	6.00	2.00	0.20	4.00	0.90	Bal.

2.2 Design

To validate the mold-filling capability and solidification integrity of ceramic preforms for high-melting metallic lattice structures fabrication, a representative structural configuration was selected for experimental verification. Theoretical analyses and numerical simulations indicate that the Kelvin cell topology exhibits superior mechanical characteristics compared to alternative architectures, making it an optimal candidate for lattice structure construction. Accordingly, this study implements a casting process optimization framework based on Kelvin cell geometry. Figure 1 illustrates the three-dimensional model of both the Kelvin unit cell and the corresponding lattice structure, with overall dimensions of 90 mm × 90 mm × 158 mm. The strut diameter varies between 3-5 mm, while the porosity is maintained within 50-90% through structural design.

Metal casting predominantly utilizes two gating configurations: top-pour and bottom-pour systems. Conventional wisdom holds that top-pour systems leverage gravitational advantages but suffer from heterogeneous thermal field distributions, predisposing to defect formation (shrinkage cavities, gas porosity, inclusions)[28]. Conversely, bottom-pour systems achieve stabilized mold filling with reduced oxide entrapment, albeit constrained by limited feeding capacity[29]. Given these complementary trade-offs, systematic investigation of gating methodologies is imperative for metallic lattice structure fabrication.

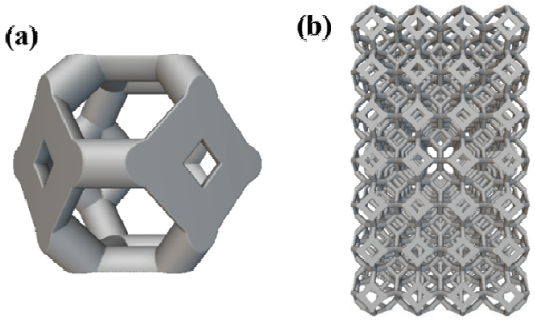

Figure. 1 (a) Kelvin unit cell (b) Kelvin lattice structure.

This study implemented a cross-sectional area ratio methodology for gating system design. In the bottom-pour configuration, the sprue-runner-ingate area ratio was maintained at 1:1.35:1.5. For an exemplar 82% porosity metallic lattice structure, the ingate cross-section measured 1256 mm², dictating runner and sprue dimensions of 85 mm×20 mm and 43mm×43mm, respectively. The top-pour system employed a 0.6 times sample-height pressure head (empirically derived) and a modulus-based riser design. Figures 2 (a) and 2(b) schematically present the optimized top- and bottom-pour systems.

2.3 Fabrication

The fabrication protocol for high-melting-point metallic lattice structures comprises four critical phases:

Phase 1: Sacrificial Template Fabrication

Polystyrene-based sacrificial templates were produced via selective laser sintering (SLS) using the following parameters: layer thickness = 0.2 mm, scan speed = 4000 mm/s, standard layer sintering temperature = 90-100°C, and critical layer sintering = 120°C.

Phase 2: Ceramic Preform Engineering

A quartz glass matrix was engineered through sequential slurry coating (11 layers), with interlayer drying (8-12 h/layer), followed by green body finishing. Subsequent calcination eliminated organic components, yielding a

cast-ready ceramic preform.

Phase 3: Casting Process Optimization

ProCAST simulations analyzed mold filling dynamics, solidification patterns, and microstructural evolution. Vacuum-assisted gravity casting was then implemented, with process parameters refined through simulation-experiment synergy.

Phase 4: Preform Removal

The ceramic preform was chemically dissolved in a pressurized autoclave (280-400°C, 0.15-0.35 MPa) using concentrated alkaline solutions.

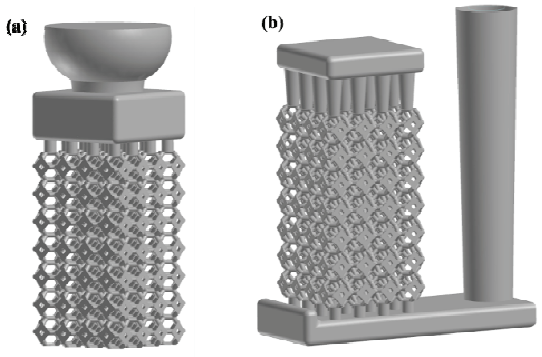

Figure. 2 Design of metallic lattice structures pouring system: (a) top pouring system; (b) bottom pouring system.

2.4 Finite element simulation

2.4.1 Casting filling and solidification simulation

The thermo-fluid dynamics governing solidification phenomena in complex castings—including heat transfer mechanisms, grain evolution, and defect formation (e.g., shrinkage porosity)—are dictated by coupled conservation equations:

Mass conservation during mold filling is expressed as:

$$\frac{\partial \rho}{\partial t}+\frac{\partial(\rho u)}{\partial x}+\frac{\partial(\rho v)}{\partial y}+\frac{\partial(\rho w)}{\partial z}=0$$

Momentum conservation follows the Navier-Stokes formulation:

$$\frac{\partial(\rho u)}{\partial t}+u\frac{\partial(\rho u)}{\partial x}+v\frac{\partial(\rho u)}{\partial y}+w\frac{\partial(\rho u)}{\partial z}$$
$$=-\frac{\partial p}{\partial x}+\mu\left(\frac{\partial^2 u}{\partial x^2}+\frac{\partial^2 u}{\partial y^2}+\frac{\partial^2 u}{\partial z^2}\right)$$
$$+\rho g_x$$

$$\frac{\partial(\rho v)}{\partial t}+u\frac{\partial(\rho v)}{\partial x}+v\frac{\partial(\rho v)}{\partial y}+w\frac{\partial(\rho v)}{\partial z}$$
$$=-\frac{\partial p}{\partial y}+\mu\left(\frac{\partial^2 v}{\partial x^2}+\frac{\partial^2 v}{\partial y^2}+\frac{\partial^2 v}{\partial z^2}\right)$$
$$+\rho g_y$$

$$\frac{\partial(\rho v)}{\partial t}+u\frac{\partial(\rho w)}{\partial x}+v\frac{\partial(\rho w)}{\partial y}+w\frac{\partial(\rho w)}{\partial z}$$
$$=-\frac{\partial p}{\partial z}+\mu\left(\frac{\partial^2 w}{\partial x^2}+\frac{\partial^2 w}{\partial y^2}\right.$$
$$\left.+\frac{\partial^2 w}{\partial z^2}\right)+\rho g_z$$

Transient heat transfer post-filling obeys Fourier's law:

$$\rho C\frac{\partial(T)}{\partial t}=\lambda\left(\frac{\partial T^2}{\partial x^2}+\frac{\partial T^2}{\partial y^2}+\frac{\partial T^2}{\partial z^2}\right)+Q$$

where u, v, w = velocity components (x,y,z); t = time; g_x, g_y, g_z = gravitational acceleration components; ρ = density; μ = dynamic viscosity; λ = thermal conductivity; C = specific heat; T = temperature; Q = volumetric heat source.

Table 4 Thermo-physical parameters, initial and boundary conditions.

Calculated parameters	Value
Solidus temperature	1235°C
Liquidus temperature	1344°C
Pouring temperature	1580°C
Pouring velocity	0.76m/s
Mold preheated temperature	900°C
Interface heat transfer coefficient	750W/(m²·K)

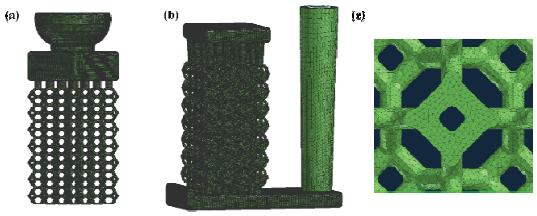

Figure. 3 The finite element mesh of the metallic lattice structures: (a) top-pouring; (b) bottom-pouring; (c) details of the mesh.

To optimize casting parameters, two gating systems were computationally evaluated using ProCAST software with tetrahedral meshing (Figure 3). Top-gated system: 475344 surface elements, 9211950 volume elements. Bottom-gated system: 655718 surface elements, 16000625 volume elements.

The test alloy used was Inconel 713 superalloy, and its thermal physical parameters were calculated using ProCAST software. Table 4 lists the thermo-physical parameters, initial conditions, and boundary conditions for the finite element simulation.

2.4.2 Casting microstructure simulation

Heterogeneous nucleation predominantly governs solidification in casting processes. Rappaz et al. established a statistical nucleation model using Gaussian distributions, where nuclei stochastically form across varying undercooling levels, with each undercooling regime activating distinct nucleation sites[30,31]. The nucleation density (n) follows a normal distribution:

$$\frac{dn}{d(\Delta T)} = \frac{n_{\max}}{\sqrt{2\pi}\Delta T_\sigma} exp\left[-\frac{(\Delta T - \Delta T_n)^2}{2\Delta T_\sigma^2}\right]$$

Where n is the grain density, n_{max} is the maximum nucleation density and contain $n_{max,S}$ and $n_{max,V}$, $n_{max,S}$ is the surface nucleation density, $n_{max,V}$ is the volume nucleation density, ΔT is total supercooling degree, ΔT_n is the mean supercooling degree, ΔT_σ is the standard deviation of the mean supercooling degree. Nucleation density under specific undercooling is quantified by:

$$n(\Delta T) = \int_0^{\Delta T} \frac{dn}{d(\Delta T)} d(\Delta T)$$

In this work, the surface nucleation density $n_{max,S}$ =1×10^5 m^{-2}, and the volume nucleation density $n_{max,V}$ = 6.35×10^8 m^{-3}.

During solidification, dendritic tip growth is thermodynamically controlled by total undercooling, and the total supercooling degree can be expressed by the equation :

$$\Delta T = \Delta T_c + \Delta T_t + \Delta T_r + \Delta T_k$$

Where, ΔT_c、ΔT_t、ΔT_r and ΔT_k correspond to solute diffusion supercooling degree, thermal diffusion supercooling degree, curvature supercooling degree, and attachment kinetics supercooling degree, respectively. The last three contributions are very small, so they can be ignored in the calculation. The growth rate of the equiaxed and columnar morphologies can be described by the KGT model [32,33].

$$v = a_2\Delta T^2 + a_3\Delta T^3$$

where, a_2 and a_3 are the growth kinetic coefficients, In this work, a_2=0 and a_3=1.86×l0^{-6}.

2.5 Characterization

Microstructural characterization employed optical microscopy (Zeiss AXIO) and micro-CT (140 μm resolution, 450 kV/1.5 mA), enabling defect analysis via 2D tomographic reconstruction. Thermal behavior was analyzed using TG-DSC (STA449 F3, NETZSCH) from 25-1550°C (10°C/min), identifying polystyrene decomposition and ceramic preform reaction temperatures to optimize sintering protocols.

3 Results and discussion

3.1 Additive Manufacturing

Fig. 4(a) displays the fabricated polystyrene lattice structure serving as sacrificial templates. The printed polystyrene exhibits a milky-white appearance with surface roughness characteristic of additive manufacturing processes. To address this limitation, a thin, smooth slurry layer was uniformly applied to the polystyrene lattice surfaces through a slurry suspension treatment at 70-80°C. This surface modification achieves three critical improvements: (1) reduction of surface roughness, (2) enhancement of mechanical strength and toughness, and (3) prevention of structural failure during subsequent ceramic preform green body fabrication. The optimized polystyrene templates after treatment (Fig. 4(b,c)) demonstrate significantly improved surface smoothness and structural integrity following the curing process, ensuring adequate dimensional stability for ceramic preform manufacturing applications.

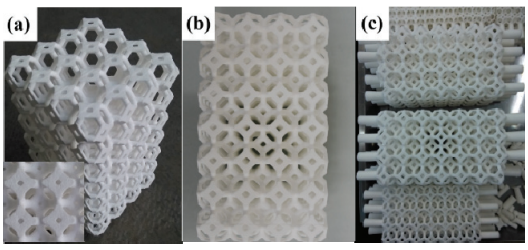

Figure. 4 Kelvin lattice structure of polystyrene fabricated by SLS: (a) As-printed; (b) Surface topography; (c) Post-treatment with hanging pulp.

3.2 High temperature resistant ceramic

The ceramic preform experiences dual thermal exposures prior to casting: (1) sintering of the green body and (2)

mold preheating during metal infiltration. Phase transformations during these thermal cycles may induce volumetric instabilities, potentially causing preform deformation or fracture. To mitigate these risks, phase evolution analysis was conducted via differential scanning calorimetry (DSC). Figure 5 compares the DSC thermograms of the first and second thermal cycles. The initial cycle exhibits thermal stability with a distinct exothermic peak at 1079.4°C, indicating crystallization (Figure 5a). Upon cooling to ambient temperature, subsequent reheating (second cycle) eliminates this exothermic event but reveals a pronounced endothermic peak at 199.5°C (Figure 5b), suggesting reversible phase transformation behavior.

Comparative analysis of the two DSC thermograms in Figure 5 reveals that thermal cycling beyond the devitrification threshold induces a low-temperature endothermic peak during secondary heating, indicating partial conversion of quartz glass to α-cristobalite [34]. Subsequent cooling transforms α-cristobalite into β-phase [35], which undergoes reversible phase transitions during reheating, manifested by the 199.5°C endotherm. Exceeding the devitrification temperature (>1079°C) during sintering promotes cristobalite formation, accompanied by ~5% volumetric strain[36,37]. This dimensional instability predisposes the preform to thermal shock-induced cracking during subsequent high-temperature exposure (casting at 1550-1650°C). To ensure structural integrity, the ceramic preform must withstand sequential thermal loads—sintering, preheating, and molten metal impingement—necessitating optimized sintering below the phase transition threshold to mitigate crystallization-driven failure.

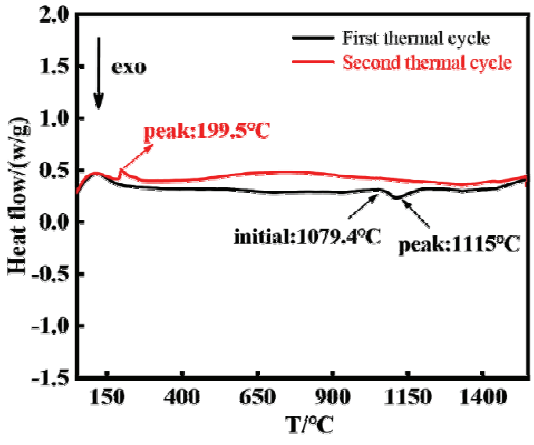

Figure. 5 The DSC curves for the first and second thermal cycles of ceramic preform.

The crystallization dynamics of quartz glass manifest temperature-dependent phase transformations requiring precise control. To modulate these structural transitions, coarse corundum sand was incorporated as a dual-functional additive. Primarily, the corundum particles act as dispersion-strengthening agents, effectively mitigating sintering-induced deformation and crack propagation through mechanical reinforcement. Secondarily, as demonstrated in literature[26], Al_2O_3 components suppress α-quartz formation by obstructing oxygen ion migration and stabilizing amorphous silica networks through Al^{3}□-Si^{4+} ionic substitution. This synergistic mechanism concurrently enhances the preform's structural homogeneity while optimizing its thermal stability. In this work, the glass transition temperature reached 1079.4℃ through the mixing of different components, which effectively improved the temperature resistance of the preform. To prevent crystal transformation, the maximum sintering temperature should not exceed 1079.4℃. Therefore, the sintering temperature of the ceramic preform was set to 1000℃ in this work.

To optimize interfacial adhesion during slurry infiltration, a surfactant-modified ceramic suspension was developed, effectively enhancing wettability of the sacrificial lattice templates. Concurrently, defoaming agents suppressed microvoid formation, complemented by sequential bubble-removal protocols: mechanical agitation, gravitational settling, and vacuum degassing. Empirical formulation trials revealed poor colloidal stability in the initial slurry, which was resolved through strategic silicon powder addition (0.5-1.5 wt%). This additive modulated rheological behavior, improved suspension homogeneity, and adjusted sintered component density.

Figure 6 presents the TG-DSC profile of laser-sintered polystyrene, revealing critical thermal transitions: glass transition (112°C), decomposition onset (380°C), peak degradation (420°C), and complete decomposition by 480°C (0% residual mass). To mitigate preform damage from rapid pyrolysis, a controlled thermal protocol was implemented: gradual heating (<5°C/min) with isothermal holding at 400°C (1 hour) to ensure progressive polymer removal.

The ceramic preform green body was fabricated through a sequential dip-coating process, wherein a ceramic slurry with a precisely controlled solid-to-liquid ratio of 3:1 [38] was systematically applied to the sacrificial lattice templates. Each dip-coating iteration

was followed by a 10-hour ambient drying phase at 25°C to ensure uniform layer consolidation. This cyclic process was repeated 11 times to achieve complete encapsulation of the three-dimensional lattice architecture by the ceramic slurry, as visually confirmed in Figure 7(a)-(b). To optimize interfacial adhesion during the impregnation stages, a tailored surfactant additive (0.1-0.2 wt%) was incorporated into the slurry formulation, significantly enhancing wettability and mitigating interfacial defects.

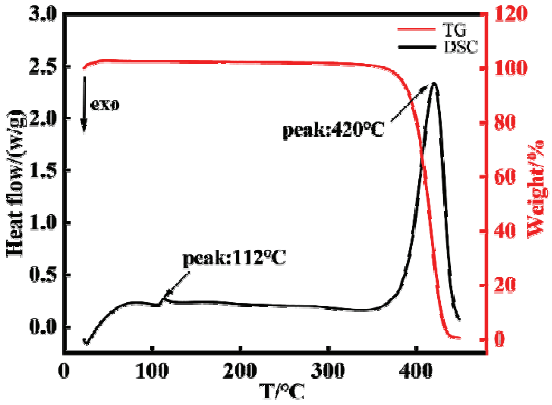

Figure. 6 TG-DSC curves of polystyrene.

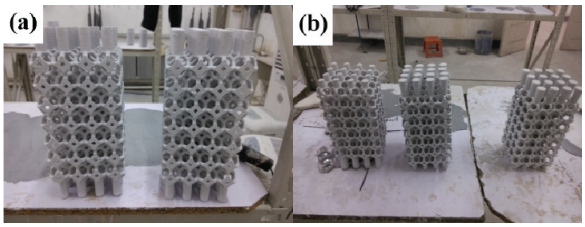

Figure. 7 Ceramic slurry covered polystyrene lattice structure.

Post-coating protocol involved conventional shell-building techniques, wherein additional refractory layers were deposited prior to the sintering process. The thermal treatment schedule (Figure 8) was strategically designed through synergistic analysis of the ceramic preform's DSC characteristics and polystyrene's TG-DSC decomposition profile. Critical thermal stages included: (1) Controlled ramp phase (from 25°C to 400°C over 6 hours): Facilitated gradual polystyrene softening while minimizing thermal shock; (2) Isothermal plateau at 400°C (1 hour): Enabled progressive polymer decomposition and gaseous byproduct evolution; (3) Oxidative elimination phase at 500°C (1 hour): Ensured complete organic template removal through thermal degradation; (4) Densification stage at 1000°C (4 hours): Promoted ceramic particle coalescence and structural consolidation. Following furnace cooling to ambient temperature, the phase-stable ceramic preform was subjected to investment casting operations, demonstrating preserved architectural fidelity and mechanical robustness required for molten metal containment.

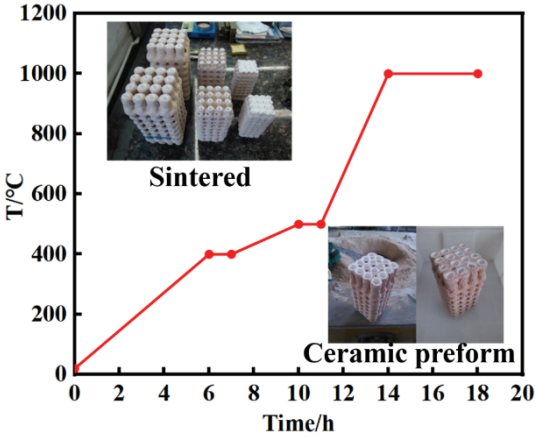

Figure. 8 Sintering curve of ceramic preform.

3.3 Investment casting

Figure 9 illustrates the mold-filling simulations for top- and bottom-gated systems. Both systems were maintained at a pouring temperature of 1580°C, with ceramic preforms preheated to 900°C. During molten metal infiltration into the lattice architecture, the intricate flow pathways predispose the process to defects such as misruns and oxide entrapment. To mitigate these risks, both gating designs incorporate restricted gates adjacent to lattice unit cells, generating backpressure to promote complete mold filling and minimize defect formation.

In the top-gated system, molten metal flows through the pouring basin into the runner, subdividing into branch channels connected to individual lattice units. Under gravitational force, the fluid exhibits a central velocity gradient with radial flow divergence, resulting in rapid mold filling and uniform thermal distribution throughout the process. Conversely, the bottom-gated system employs progressive filling dynamics: liquid metal initially accumulates in the runner until achieving critical hydraulic head, then ascends through multiple feed channels to fill the lattice sequentially from base to apex. This counter-gravity approach suppresses free-surface turbulence, enhancing flow stability and promoting directional solidification. Numerical simulations demonstrate complete mold filling in both systems, with the bottom-gated configuration exhibiting superior flow uniformity (Figure 9).

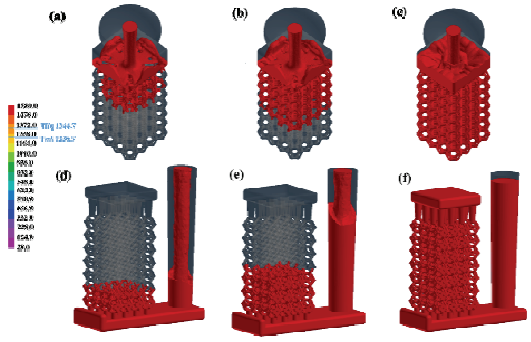

Figure. 9 Pouring velocity field of two pouring methods: (a) top pouring; (b) bottom pouring.

During solidification, high-temperature molten metal dissipates thermal energy through thermal conduction, radiation, and convective transfer to the mold and ambient environment, progressively solidifying into metallic lattice architectures[34]. The thermal profiles following mold filling for both gating configurations are depicted in Figure 10. Throughout solidification, temperature fields exhibit homogeneous distribution, with both methodologies demonstrating near-synchronous solidification across lattice elements. This coordinated phase transformation minimizes thermal gradients, thereby facilitating isotropic mechanical properties in the final metallic lattice structures.

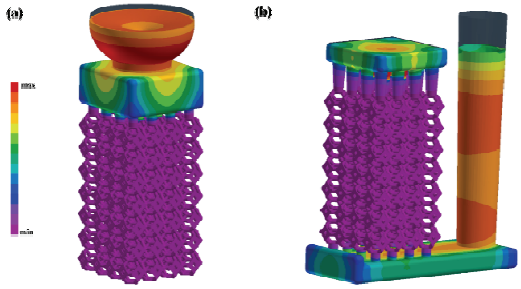

Figure. 10 Solidification characteristics of two pouring methods: (a) top pouring; (b) bottom pouring.

Computational simulations indicate that a preheating temperature of 900°C enables complete mold filling at 1580°C, though ProCAST's inherent limitations preclude definitive prediction of structural fidelity. To refine process parameters, orthogonal experimentation was conducted across three critical variables: casting temperature (1550-1650°C), mold preheating (900-1000°C), and pore-strut diameter (3-5 mm). Filling efficiency (defined as actual filling distance-to-height ratio) served as the evaluation metric, with experimental outcomes detailed in Table 5.

Table 5 $L_9(3)^4$ Orthogonal experiment table of casting process.

Factor	Pouring set temperature（℃）	Preheating temperature（℃）	Rod diameter（mm）	Pouring mode	Filling Ratio(%)
1	1550	900	3	Top	100
2	1550	950	4	Bottom	83
3	1550	1000	5	Top	100
4	1600	900	4	Top	100
5	1600	950	5	Top	100
6	1600	1000	3	Bottom	75
7	1650	900	5	Bottom	90
8	1650	950	3	Top	100
9	1650	1000	4	Top	100

Analysis of Table 5 reveals the pouring methodology exerts a pronounced influence on mold-filling efficacy. The top-gated system achieves complete cavity filling across the tested parameter ranges (casting temperature: 1550–1650°C; preheating: 900–1000°C; pore-strut diameter: 3–5mm). Conversely, the bottom-gated configuration demonstrates markedly inferior performance, with filling efficiencies ranging from 75% to 90% under optimal conditions (1650°C casting temperature, 900°C preheating, 5mm strut diameter). This observed discrepancy between experimental and simulated outcomes stems from fundamental flow dynamics: Gravity-driven flow in the top-gated system enhances metal delivery, whereas reduced filling velocities in the bottom-gated approach limit cavity penetration completeness.

Experimental validation confirms that the top-gated system (casting temperature: 1550 °C; mold preheating: 900 °C) achieves complete infiltration of 3 mm struts, as evidenced by the pre-/post-casting samples in Figures 11a–e. Post-solidification analysis reveals intimate ceramic-metal interpenetration within the lattice network.

Subsequent chemical dissolution successfully eliminates residual ceramic material, yielding a defect-free metallic lattice (Figure 11f) with smooth surface topology. This demonstrates the preform's exceptional removability and structural fidelity, validating its suitability for high-melting-point metallic lattice fabrication.

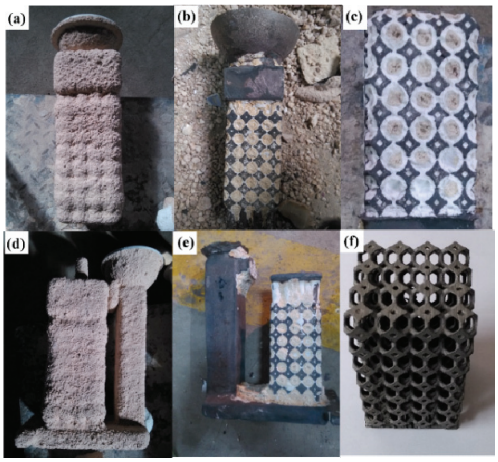

Figure. 11 (a)-(c) The result of top pouring, (d)-(e) bottom pouring, (f) In713 metallic lattice structure after ceramic removal.

3.4 Microstructure

To comprehensively assess the fabricated high-melting-point metallic lattice, microstructural and defect analyses were conducted. Figure 12 presents ProCAST-predicted shrinkage distributions for the two casting methodologies. Both systems exhibit significant defect formation at lattice node junctions — regions of strut interconnection. Solidification-induced liquid shrinkage occurs in terminally solidified zones due to geometric complexity, while structural constraints prevent effective shrinkage compensation, resulting in isolated liquid pools and final-stage shrinkage cavities. Although feeding strategies can mitigate such defects, the lattice architecture inherently limits timely melt replenishment at nodal junctions.

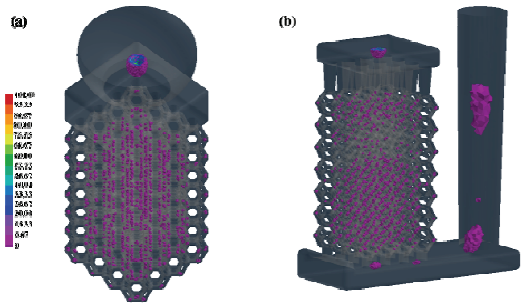

Figure. 12 Prediction of total shrinkage porosity of castings: (a) top pouring; (b) bottom pouring.

Figure 13 (a) presents a cross-sectional analysis of defect localization predicted by ProCAST, highlighting preferential defect nucleation at nodal junctions. To validate simulation accuracy, complementary experimental techniques—micro-CT non-destructive evaluation and destructive sectioning analysis—were implemented. Figure 13 (b) demonstrates remarkably congruent defect distributions between simulated and micro-CT results, with both methods identifying pronounced shrinkage porosity at strut intersections. Physical cross-sectioning (Figure 13(c)) further corroborates cavity formation at these critical nodes, collectively confirming inherent solidification challenges in lattice casting, and the validity of simulation parameters in replicating actual defect mechanisms.

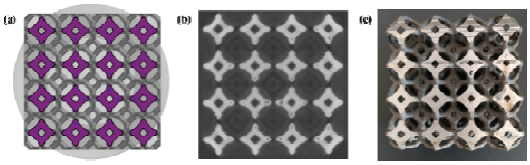

Figure. 13 The position of shrinkage porosity: (a) simulated slice; (b) Micro-CT slice; (c) real surface.

Figure 14 (a) illustrates the numerical prediction of grain morphology in the metallic lattice structure via ProCAST's CAFE method, while Figures 14 (b-c) present experimentally characterized microstructures. Comparative analysis reveals consistent grain uniformity between simulation and experimental observations. Simulated grains exhibit an average diameter of 723.8 μm, slightly smaller than the experimentally measured 838.26 μm. Despite this minor discrepancy, the simulated grain topology and size distribution align closely with optical microscopy results, validating the applicability of the CAFE model with optimized nucleation parameters and growth kinetics coefficients for predicting solidification microstructure evolution in metallic lattice architectures.

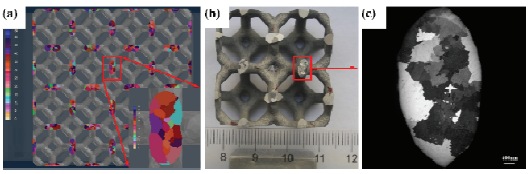

Figure. 14 Grain structure of Kelvin lattice structure after casting: (a) Grain structure simulated by CAFE model; (b) Lattice structure after cutting; (c) Microstructure of as-cast Inconel 713.

4 Conclusions

This study demonstrates the first successful fabrication of

high-melting metallic lattice structures through additive manufacturing assisted investment casting. Key advancements include:

(1) A hybrid process integrating selective laser sintering and investment casting enables laboratory-scale production of metallic lattice structures with superior high-temperature performance (enhanced thermal resistance, corrosion resistance, strength, and stiffness) compared to low-melting-point counterparts, while reducing production costs to broaden industrial applicability.

(2) A novel quartz glass-based ceramic preform sintered below 1000°C was developed, exhibiting excellent thermal stability and post-casting removability, making it fully compatible with high-melting-point metallic lattice structure fabrication.

(3) Comparative analysis of gating systems via orthogonal experiments and finite element simulations identified top pouring (1550°C pouring temperature, 900°C mold preheating) as the optimal method for producing Kelvin-type Inconel 713 metallic lattice structures.

(4) Multi-modal defect characterization (ProCAST, micro-CT, sectioning) confirmed simulation-predicted shrinkage porosity concentrated at strut-node junctions—an inherent limitation of lattice solidification. CAFE-modeled grain structures aligned with experimental observations, validating the model's utility for casting process optimization.

This methodology establishes a scalable pathway for manufacturing complex high-performance metallic lattice structures, overcoming traditional limitations in high-temperature casting while expanding design flexibility for aerospace and energy applications.

Acknowledgments

This work was financially supported by the Liaoning Province Applied Fundamental Research Program (No. 2023JH2/101700039) and Liaoning Province Natural Science Foundation (No. 2023-MSLH-328).

Conflicts of interest:

The authors declare that they have no known competing financial interests or personal relationships that could have appeared to influence the work reported in this paper.

References

[1] Sajjad U, Rehman T, Ali M, Park CW, Yan W-M. Manufacturing and potential applications of lattice structures in thermal systems: A comprehensive review of recent advances. International Journal of Heat and Mass Transfer, 2022, 198: 123352.

[2] Sugimura Y, Meyer J, He MY *et al.* On the mechanical performance of closed cell Al alloy foams. Acta Materialia, 1997, 45: 5245–5259.

[3] Großmann A, Gosmann J, Mittelstedt C. Lightweight lattice structures in selective laser melting: Design, fabrication and mechanical properties. Materials Science and Engineering: A, 2019, 766: 138356.

[4] Shen M, Qin W, Xing B *et al.* Mechanical properties of 3D printed ceramic cellular materials with triply periodic minimal surface architectures. Journal of the European Ceramic Society, 2021, 41: 1481–1489.

[5] Xiao Z, Yang Y, Xiao R et al. Evaluation of topology-optimized lattice structures manufactured via selective laser melting. Materials & Design, 2018, 143: 27–37.

[6] Ghanavati R, Naffakh-Moosavy H, Moradi M, Eshraghi M. Printability and microstructure of directed energy deposited SS316l-IN718 multi-material: numerical modeling and experimental analysis. Scientific Reports, 2022, 12: 16600.

[7] Shah M, R.Patel D, Pande S. Additive manufacturing integrated Casting- A review. Materials Today: Proceedings, 2022, 62: 7199–7203.

[8] Carneiro VH, Rawson SD, Puga H, Meireles J, Withers PJ. Additive manufacturing assisted investment casting: A low-cost method to fabricate periodic metallic cellular lattices. Additive Manufacturing, 2020, 33: 101085.

[9] Mun J, Yun B-G, Ju J, Chang B-M. Indirect additive manufacturing based casting of a periodic 3D cellular metal – Flow simulation of molten aluminum alloy. Journal of Manufacturing Processes, 2015, 17: 28–40.

[10] Pinto P, Peixinho N, Silva F, Soares D. Compressive properties and energy absorption of aluminum foams with modified cellular geometry. Journal of Materials Processing Technology, 2014, 214: 571–577.

[11] Shangguan H, Kang J, Deng C, Hu Y, Huang T. 3D-printed shell-truss sand mold for aluminum castings. Journal of Materials Processing Technology, 2017, 250: 247–253.

[12] Gallien F, Gass V, Mortensen A. Investment casting of periodic aluminum cellular structures using slurry-cast table salt moulds. Materials & Design, 2022, 215: 110488.

[13] Xue Y, Wang X, Wang W, Zhong X, Han F. Compressive property of Al-based auxetic lattice structures fabricated by 3-D printing combined with investment casting. Materials Science and Engineering: A, 2018, 722: 255–262.

[14] Nazir A, Gokcekaya O, Md Masum Billah K et al. Multi-material additive manufacturing: A systematic review of design, properties, applications, challenges, and 3D printing of materials and cellular metamaterials. Materials & Design, 2023, 226: 111661.

[15] Srivastava M, Rathee S, Patel V, Kumar A, Koppad PG. A review of various materials for additive manufacturing: Recent trends and processing issues. Journal of Materials

Research and Technology, 2022, 21: 2612–2641.
[16] Shakil SI, Zoeram AS, Pirgazi H et al. Microstructural-micromechanical correlation in an Al–Cu–Mg–Ag–TiB2 (A205) alloy: additively manufactured and cast. Materials Science and Engineering: A, 2022, 832: 142453.
[17] Snelling D, Li Q, Meisel N et al. Lightweight Metal Cellular Structures Fabricated via 3D Printing of Sand Cast Molds. Advanced Engineering Materials, 2015, 17: 923–932.
[18] 1 Kang J, Shangguan H, Deng C et al. Additive manufacturing-driven mold design for castings. Additive Manufacturing, 2018, 22: 472–478.
[19] Huang Y, Xue Y, Wang X, Han F. Mechanical behavior of three-dimensional pyramidal aluminum lattice materials. Materials Science and Engineering: A, 2017, 696: 520–528.
[20] Qiao M, Li X, Chen P, Zhu Y, Zhu B. Pore evolution and slag resistance of corundum castables with nano zirconia addition. Ceramics International, 2021, 47: 6947–6954.
[21] Chang Y, Yao X, Chen Y, huang L, Zou D. Review on ceramic-based composite phase change materials: Preparation, characterization and application. Composites Part B: Engineering, 2023, 254: 110584.
[22] Kanyo JE, Schafföner S, Uwanyuze RS, Leary KS. An overview of ceramic molds for investment casting of nickel superalloys. Journal of the European Ceramic Society, 2020, 40: 4955–4973.
[23] Ignatova AM, Vereschagin VI, Naimark OB. Features of crystallization of cast glass-ceramic spinel-pyroxene materials under non-equilibrium conditions. Procedia Structural Integrity, 2022, 41: 527–534.
[24] Chen X, Zhou Y, Jin T, Sun X. Effect of C and Hf Contents on the Interface Reactions and Wettability between a Ni3Al-Based Superalloy and Ceramic Mould Material. Journal of Materials Science & Technology, 2016, 32: 177–181.
[25] Jin L, Guo J-F, Luo Y-J, Zhou Z, Chen S. Tuning high and low thermal expansion coefficients of Li2O–BaO–Al2O3–B2O3–SiO2/quartz LTCC composites by replacing quartz partly with α-Al2O3 or ZrO2. Ceramics International, 2022, 48: 37353–37361.
[26] Wang Y, Liu Q, Zhang B et al. Microstructure and mechanical behaviour of transient liquid phase spark plasma sintered B4C–SiC–TiB2 composites from a B4C–TiSi2 system. Ceramics International, 2021, 47: 10665–10671.
[27] Boutarek N, Saïdi D, Acheheb MA, Iggui M, Bouterfaïa S. Competition between three damaging mechanisms in the fractured surface of an Inconel 713 superalloy. Materials Characterization, 2008, 59: 951–956.
[28] Pattnaik S, Karunakar DB, Jha PK. Developments in investment casting process—A review. Journal of Materials Processing Technology, 2012, 212: 2332–2348.
[29] Reilly C, Green NR, Jolly MR. The present state of modeling entrainment defects in the shape casting process. Applied Mathematical Modelling, 2013, 37: 611–628.
[30] Rappaz M, Gandin Ch-A. Probabilistic modelling of microstructure formation in solidification processes. Acta Metallurgica et Materialia, 1993, 41: 345–360.
[31] Thévoz Ph, Desbiolles JL, Rappaz M. Modeling of equiaxed microstructure formation in casting. Metallurgical Transactions A, 1989, 20: 311–322.
[32] Lipton J, Glicksman ME, Kurz W. Dendritic growth into undercooled alloy metals. Materials Science and Engineering, 1984, 65: 57–63.
[33] Kurz W, Giovanola B, Trivedi R. Theory of microstructural development during rapid solidification. Acta Metallurgica, 1986, 34: 823–830.
[34] Li H, Hu K, Liu Y, Lu Z, Liang J. Improved mechanical properties of silica ceramic cores prepared by 3D printing and sintering processes. Scripta Materialia, 2021, 194: 113665.
[35] Kazemi A, Faghihi-Sani MA, Alizadeh HR. Investigation on cristobalite crystallization in silica-based ceramic cores for investment casting. Journal of the European Ceramic Society, 2013, 33: 3397–3402.
[36] Krug S, Evans JRG, ter Maat JHH. Residual stresses and cracking in large ceramic injection mouldings subjected to different solidification schedules. Journal of the European Ceramic Society, 2000, 20: 2535–2541.
[37] Wilson PJ, Blackburn S, Greenwood RW, Prajapti B, Smalley K. The role of zircon particle size distribution, surface area and contamination on the properties of silica–zircon ceramic materials. Journal of the European Ceramic Society, 2011, 31: 1849–1855.
[38] Venkat Y, Choudary KRS, Das DK, Pandey AK, Singh S. Alumina-zircon filler based ceramic shell moulds for directionally solidified cast shrouded low pressure turbine blades. Ceramics International, 2021, 47: 27395–27405.